Already have a manuscript?

Use our Manuscript Matcher to find the best relevant journals!

Find a Match

Filters Clear All

Web of Science Coverage

Core Collection

- [x] Science Citation Index Expanded (SCIE)
- [x] Social Sciences Citation Index (SSCI)
- [x] Arts & Humanities Citation Index (AHCI)
- [x] Emerging Sources Citation Index (ESCI)

Current Contents

- [ ] Agriculture, Biology & Environmental Sciences

Refine Your Search Results

Scientific report

Search

Sort By: Relevancy

Active Filters

SCIENCE CITATION INDEX EXPANDED (SCIE) × SOCIAL SCIENCES CITATION INDEX (SSCI) × ARTS & HUMANITIES CITATION INDEX (AHCI) × EMERGING SOURCES CITATION INDEX (ESCI) ×

Search Results

Found 12,658 results (Page 1) Share These Results

Did you mean this journal?

SCIENTIFIC REPORTS

Publisher: **NATURE PORTFOLIO , HEIDELBERGER PLATZ 3, BERLIN, Germany, 14197**

ISSN / eISSN: **2045-2322**

Web of Science Core Collection: **Science Citation Index Expanded**

Additional *Web of Science* Indexes: **Biological Abstracts | BIOSIS Previews | Current Contents Physical, Chemical & Earth Sciences | Essential Science Indicators | Zoological Record**

Open Access

Scientific Reports

Springer Nature ISSN: 20452322 Journal publications in Cobalt

Are you a researcher?

Create a profile to get free access to personal recommendations for colleagues and new articles.

Login with ORCID

ALL TIME **FROM 2021**

Publications	Citations	*h*-index
275 752	**5 984 706**	**377**

TOP-3 CITING JOURNALS

- Scientific Reports (212626 citations)
- International Journal of Molecular Sciences (89396 citations)
- PLoS ONE (45227 citations)

SCIMAGO **WOS**

Q1 Q1

Impact factor
3.9

SJR
0.874

CiteScore
6.7

Categories
Multidisciplinary

TOP-3 ORGANIZATIONS

ALL TIME **IN 5 YEARS**

- French Institute of Health and Medical Research (3160 publications)
- University of Tokyo (3155 publications)
- Harvard University (3119 publications)

TOP-3 COUNTRIES

ALL TIME **IN 5 YEARS**

- China (54687 publications)
- USA (49496 publications)
- Japan (20621 publications)

scientific reports

Check for updates

OPEN

Middle Pleistocene tectonic events around the SE Aegean Sea: Insights from magnetostratigraphy, (U–Th)/He zircon dating, and fault kinematics in the Datça Graben (SW Türkiye)

Meryem Dilan İnce[1], Nuretdin Kaymakci[1,2]✉, Cor Langereis[3], Bora Uzel[4], Erhan Gülyüz[2,5], Ersin O. Koralay[4], Marius Stoica[6] & Ökmen Sümer[4]

This study constrains the stratigraphy, age, and tectono-sedimentary evolution of the Datça Graben (southwestern Turkey) through integrated magnetostratigraphy, zircon (U-Th)/He geochronology, sedimentological analysis, and fault kinematic studies. The basin, developed along the southwestern margin of Anatolia under N-S extension, preserves ~ 350 m of fluvio-lacustrine to shallow-marine deposits, primarily assigned to the Yıldırımlı Formation. Two interbedded tuff layers yield zircon (U-Th)/He ages of 1.56 ± 0.10 Ma and 1.44 ± 0.10 Ma, constraining deposition between 1.78 and 0.78 Ma (Calabrian Age) when correlated to the Geomagnetic Polarity Time Scale. Magnetostratigraphy records a reversed-normal-reversed polarity sequence within subchrons C1r.2r, C1r.1n, and C1r.1r. The basin fill dips southward, with thicker accumulations along the southern boundary fault, indicating an asymmetric half-graben geometry dominated by southern-margin subsidence. Syn-depositional growth faults, paleostress analysis, and mesoscopic fault kinematics indicate persistent N-S extension with minor azimuthal variations (NNW-SSE to NE-SW). Paleomagnetic declination data reveal ~ 13° ± 5° counterclockwise rotation since the Calabrian, supporting differential rotation across the Datça Peninsula and linking basin development to progressive opening of the Gökova Basin. Sedimentological evidence documents initial fluvio-lacustrine conditions, followed by a shallow-marine transgressive phase, with the upper marine deposits now > 100 m above present sea level, implying significant post 0.78 Ma uplift. Uplift and facies associations suggest dynamic topography and slab-edge processes associated with STEP faulting along the Pliny-Strabo Trenches controlled the evolution of the basin. Our results provide the most precise chronological framework to date for the Datça Graben, refine its structural development, and constrain the timing of Gökova Basin opening to post-1 Ma. The integration of magnetostratigraphic, geochronological, and structural datasets sheds light on the understanding of Aegean extensional dynamics and the interplay between regional rotation, uplift, and marine connectivity during the Quaternary.

Keywords Datça Graben, Extensional tectonics, Magnetostratigraphy, Thermochronological dating, Kinematic analysis, Gökova Basin

[1]Department of Geological Engineering, Middle East Technical University (METU), Dumlupınar Bulvarı 1, 06800 Ankara, Turkey. [2]Department of Neotectonics and Thermochronology, Institute of Rock Structure and Mechanics of the Czech Academy of Science, V Holesovickach 94/41, 182 09 Prague 8, Czech Republic. [3]Department of Earth Sciences, Utrecht University, Budapestlaan 17, 3584 CD Utrecht, the Netherlands. [4]Department of Geological Engineering, Dokuz Eylül University, Tınaztepe Campus, 35160 İzmir, Turkey. [5]Department of Geological Engineering, Van Yüzüncüyıl University, TR-65080 Van, Turkey. [6]Geology and Geophysics, University of Bucharest, 050107 Bucharest, Romania. ✉email: kaymakci@metu.edu.tr

The Aegean and southwestern Anatolia region is key to understanding extensional deformation related to slab-edge processes, including subduction roll-back and STEP faulting. These processes govern deformation in the overlying plate, leading to crustal stretching, thinning, and dynamic topography, which, in turn, gave way to sea-level fluctuations, basin formation, and sediment deposition. Since the late Oligocene, the Aegean region has experienced vertical motions and block rotations, resulting in complex fault patterns and kinematics[1–7].

While the primary drivers of these vertical motions remain debated, various scenarios have been proposed. One key hypothesis is escape tectonics, which posits that the westward motion of the Anatolian Block, along the dextral North Anatolian and sinistral East Anatolian transform faults, results from the collision and convergence of the Arabian plate, creating a zone of high strain. This westward motion induces E-W compression and N-S extension[8–10]. However, the onset of extension predates the escape tectonics, limiting its relevance to post-late Miocene evolution. The southward retreat of the northward-subducting African lithosphere since the early Miocene is widely regarded as the dominant mechanism driving extensional deformation[1,11–14].

Recent studies, supported by mantle tomography[15–19], suggest that lithospheric tearing led to the development of asymmetric slab rollback and Subduction Transform-Edge Propagator (STEP) faulting[20], which contributed to differential vertical motions and block rotations in the Aegean Sea region and western Anatolia, since the late Oligocene[6,7,21–25]. This process appears to have accelerated during the Late Pliocene[26,27]. The tear in the African slab also facilitated the formation of STEP faults along the Pliny-Strabo Trenches, a sinistral shear zone contributing to the westward motion and counterclockwise rotation of western Anatolia[6,14,17,28,29].

The main cause of debate regarding the precise timing and mechanism of extension in western Anatolia is largely related to the scarcity of long and continuous stratigraphical sections and precise dating. Inception ages are often based on the onset of continental deposition in extension-related basins[4] and thermochronological data on the exhumation of metamorphic rocks related to regional extension and detachment faulting[30,31]. The sedimentary record is primarily characterized by continental clastics deposited on exhumed metamorphic rocks and un- or partially metamorphosed hanging-wall blocks above detachment faults[5,32–34], dating back to the early Miocene[6]. During the middle Miocene, large but isolated lacustrine systems, intercalated with bimodal volcanism, characterized the region, with volcanic activity migrating southward as the subducted Aegean slab retreated[22]. Recent studies[35,36] indicate that the Aegean-west Anatolian region was dominated by fluvio-lacustrine conditions during the late Miocene, with the Aegean Sea largely disconnected from the Mediterranean, except for its southernmost part north of Crete, potentially until the Pliocene (Fig. 1). Meanwhile, the northern Aegean basin remained connected to the eastern Paratethys via the Dardanelles[35,37,38].

Studies of late Pliocene to Quaternary deposits[39,40] suggest that the southeastern Aegean was intermittently inundated, with marine deposits exposed in the eastern part of Rhodes Island, the Datça Peninsula, and Kos Island, indicating temporary inundation of the region during the middle Pleistocene[41–47]. However, these exposures are limited, and the extent and timing of marine transgression in the Aegean Sea remain uncertain, largely due to the restricted availability of marine deposits across the basin. Notably, Datça Peninsula (Fig. 1) contains over 350 m of basin fill, comprising fluvio-lacustrine deposits interbedded with marine facies. On the other hand, Lykousis[48] claimed that large areas of the Aegean seafloor that are presently at 400 m depth, were exposed during the low sea-level stages MIS 10 and 12, roughly 350–480 kyr BP. Due to ongoing tectonic subsidence, it is expected that even deeper parts of the Aegean seafloor may have been exposed during the Calabrian Age.

The goal of this study is to establish the precise age of continental and marine sequences within the Datça Graben using integrated stratigraphic tools, including magnetostratigraphy, thermochronology, facies analysis, and field observations. These results will quantify deposition rates, provide constraints on vertical motions in the region, and shed light on the temporal evolution of Gökova Bay and the adjacent marine areas. A detailed fault kinematic analysis is also conducted to examine the interaction between sedimentation and faulting.

Regional setting and Datça Graben

E-W trending Datça Peninsula is located on the southwestern edge of the Anatolian Peninsula. It is surrounded by the Dodecanese islands and delimits the Gökova Bay in the north (Fig. 2). There is a noticeable depression in the central part of the peninsula. Both the northern and southern margins of the depression are faulted, giving rise to Datça Graben[49]. The present geometry of the basin infill is exposed as rolling hills at the central part of the depression. In general, the basin infill deposits gently dip southwards about ~ 15–20° degrees (Fig. 2c). The southern boundary block of the graben is topographically higher than the northern block and the peaks reach up to 1100 m elevations.

Stratigraphy

The stratigraphic units exposed in the Datça Peninsula are subdivided into two groups. These are basin infill units and pre-Pliocene basement units (Fig. 2b). The basement rocks comprise various thrust slices of the Lycian Nappes comprising dismembered slices of ultramafic, mafic, and magmatic rocks as well as epi-ophiolitic deep sea mudstones and radiolarites set in upper Cretaceous ophiolitic mélange structurally overlying upper Cretaceous turbidites. Ophiolitic mélange is tectonically overlain by Upper Triassic-Lower Jurassic platform carbonates and tectonic slices of upper Jurassic-upper Cretaceous radiolarites and cherty limestones. All of the Mesozoic lithologies and tectonic slices are unconformably overlain by the Plio-Quaternary infill of the Datça Graben[49,50].

Basin infill

The basin infill units of the Datça Graben comprise from bottom to top the Kızılağaç Formation Yıldırımlı Formation, Karaköy Formation, and alluvium (Fig. 2). Other Quaternary units around the basin include Yazıköy

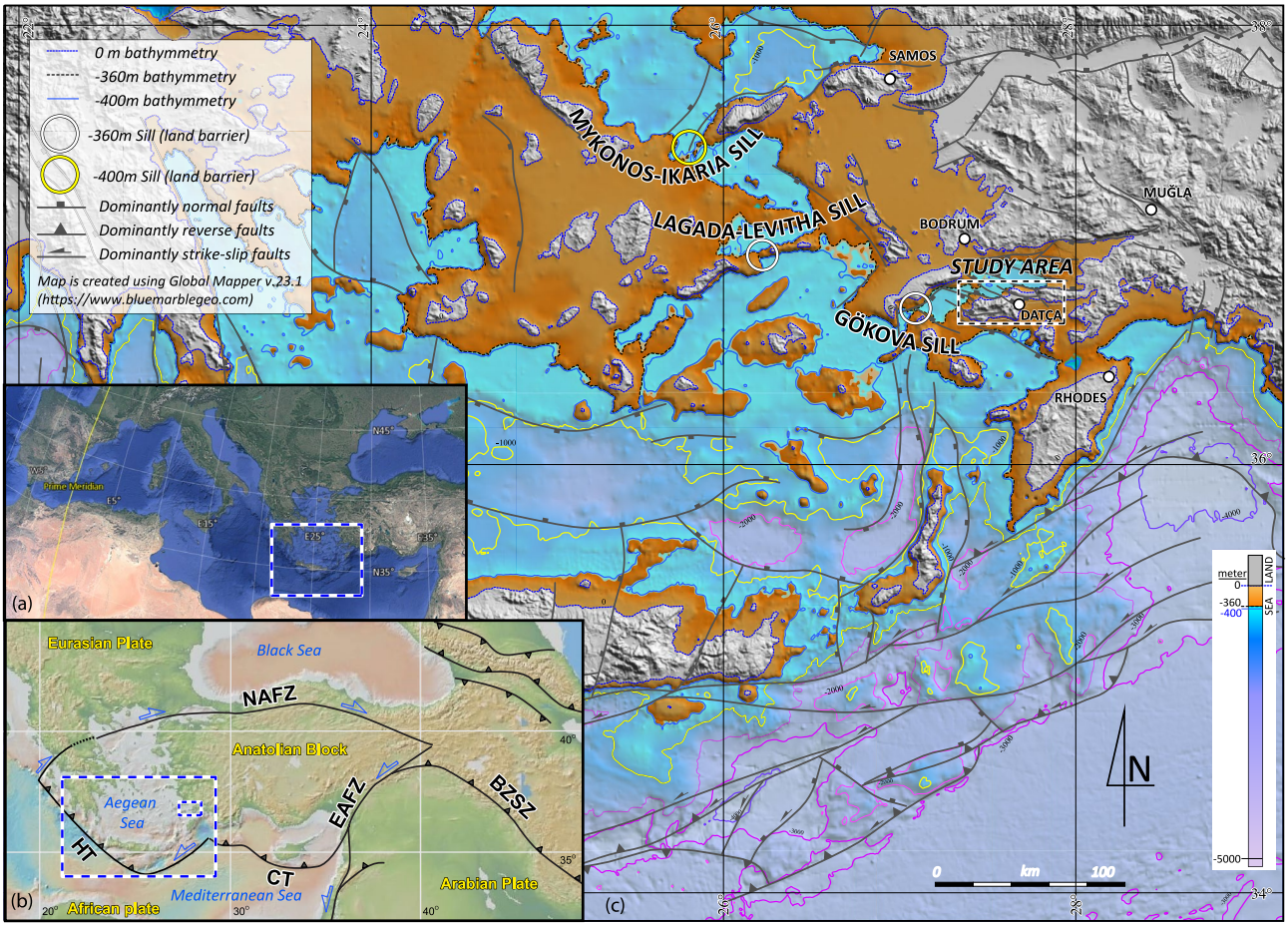


Fig. 1. (**a**) Location of the study area in the Mediterranean region. (**b**) Major tectonic structures around the Eastern Mediterranean Region. AT: Aegean Trench, BZSZ: Bitlis-Zagros Suture Zone, CT: Cyprus Trench, EAFZ: East Anatolian fault Zone, NAFZ: North Anatolian Fault Zone. (**c**) Major tectonic structures in the South Aegean-SW Anatolian Region overlaid on shaded and coloured bathymetry and topographic images. −400 and −360 m bathymetric contours and related sills are highlighted. The sills correspond to possible land bridges at 360 and 400 m depths possible during Calabrian (ca. 1 Ma). The off-shore faults are interpreted from the bathymetry and compiled from Leite and Mascle[86], Ten Veen and Kleinspeh[87]; Ganas et al.[88]; Tosun et al.[24], Özkaptan et al.[7]. Bathymetric and topographic data is obtained from Gridded Bathymetric data from GEBCO-General Bathymetric Chart of the Oceans[89]. Map was created using Global Mapper v.23.1[90].

pyroclastics, actively developing alluvial terrace deposits, colluvium, talus, alluvial fans, beach sand and gravel, and alluvium deposits.

Kızılağaç formation The Kızılağaç Formation is exposed on the northern side of the Datça Graben (51) and it is well-exposed in the northwestern part of Kızlan village (Fig. 3a). The unit unconformably overlies the ophiolitic mélange (Fig. 3b,c). at the northeast and the massive carbonates of Lycian Nappes at the northwest. The sequence starts with a polygenic conglomerate, pebbles of which derived from peridotites and limestones cemented by carbonates. Near Kızılağaç Hill located on the northwestern edge of the Datça Graben consists of limestone pebbles only indicating that pebbles are derived from underlying Mesozoic limestones (Fig. 2). So far, no biostratigraphic or any other dating information is obtained from the formation. However, based on its stratigraphic position, Ersoy[49] proposed that the age of the Kızılağaç Formation is early Pliocene.

Yıldırımlı formation The Yıldırımlı Formation[51] is the most widespread and thickest unit of the Datça Graben. The lower parts of the Yıldırımlı Formation display frequent lithological variations along the northern margin of the graben. At the west of Kızlan village, the sequence consists of ophiolite and chert pebbles cemented by carbonates, while eastwards, it is changed into thick-bedded, white-coloured oolitic limestone of lacustrine origin. Further east along the northern boundary of the graben, oolitic, pisolitic, and oncolytic limestones dominate[49].

In the western part of the graben around Körmen harbour (Fig. 2), the unit starts at the bottom with a conglomerate, sandstone, and marl alternation. Conglomerates are composed of pebbles of serpentine, gabbro, and radiolarites. Sandstone beds are interlayered with yellow-beige and grey marl and claystone levels with abundant fossil assemblages. Yıldırımlı Formation also contains a grey-coloured tuff layer near the Yıldırım

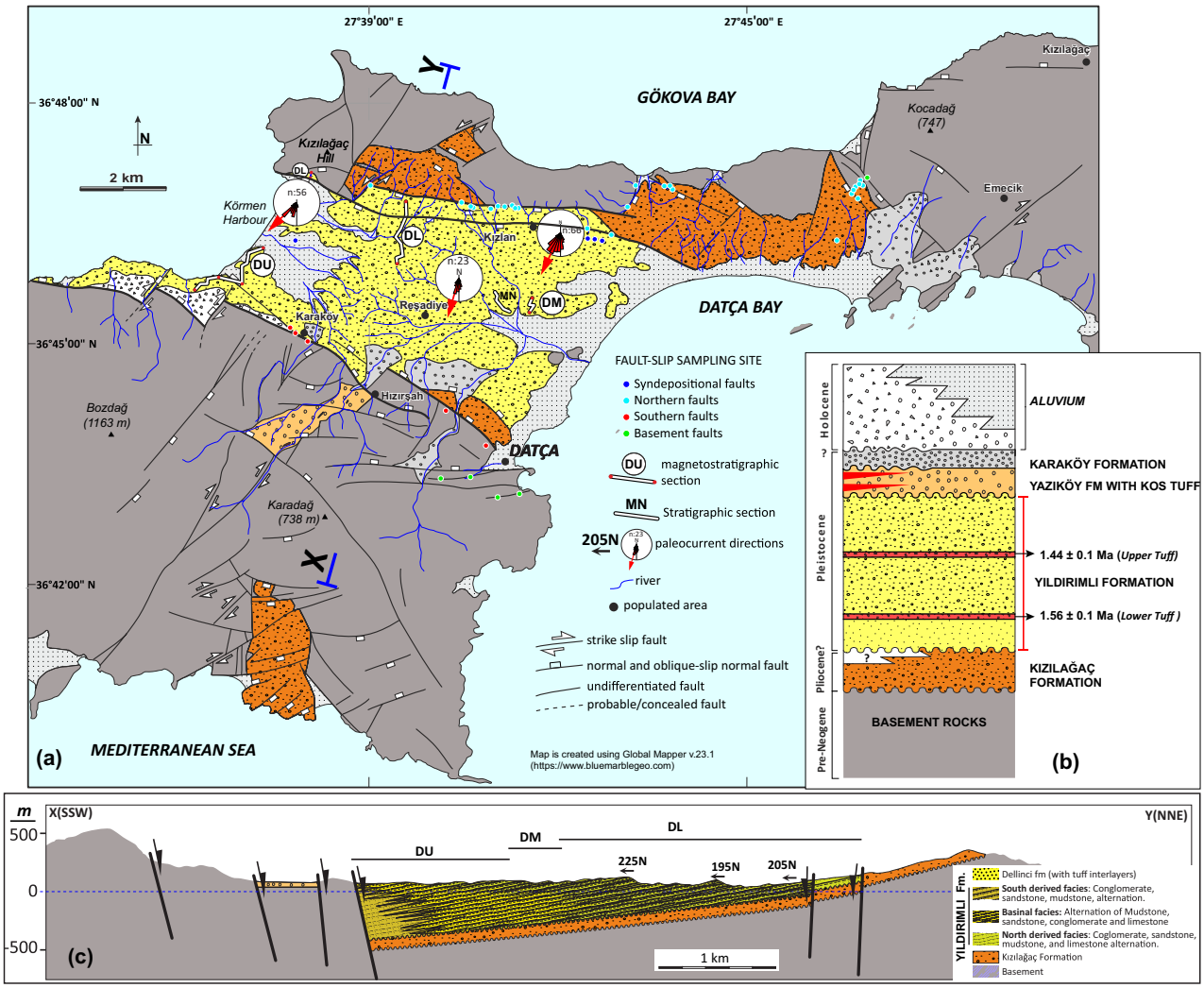


Fig. 2. (**a**) Geological map of the Datça Graben depicting structural elements, paleocurrent directions, stratigraphic sections, and kinematic sampling sites. (**b**) Generalized columnar section of the Datça Graben (Magnetostratigraphy section is shown with a red line). (**c**) Cross-section along the line XY. Note the southwards thickening and tilting of the Yıldırmlı Formation. Note also Kızılağaç Formation extends into Gökova Bay in places. Map was created using Global Mapper v.23.1[90].

Hill. The unit grades into the lacustrine deposits upwards and they are composed of conglomerate, sandstone, mudstone, claystone, marl, limestone, and rare dolomites (Fig. 3d). The depositional setting of the Yıldırımlı Formation is common in the region. It is correlated with the lower part of the Sgourou Formation[52] and Kritika Formation[41,42,53,54] of fluvio-lacustrine facies in Rhodes Island (Supplement A). The lacustrine depositional environment in the Datça Graben was first reported by Kaaden and Metz[55] based on macrofossils collected from the northwestern part of Hızırşah village. The fluvio-lacustrine deposition is followed by shallow marine river-delta slope deposits in the upper levels of the Yıldırımlı Formation. Also based on the mollusc fauna, the late Piacenzian age was attributed to Yıldırımlı Formation[56]. In addition to given ages, Electron Spin Resonance (ESR) dating resulted in a 1.891–1.998 Ma for the age of the Yıldırımlı Formation[56].

Based on these data, the lateral and vertical lithological variations indicate that the fluvio-lacustrine depositional environment is dominant in Datça Graben, and it is followed by rapid marine transgression and sudden regression.

Yazıköy formation and pyroclastics Yazıköy Formation was first named by Dirik[57] and is well-exposed in the valleys and coastal areas in Datça Peninsula (Fig. 2). It includes pyroclastic layers source of which can be attributed to the end of the modern Aegean volcanic arc extending from Greek coasts to Turkey[58]. The pyroclastics within the Yazıköy Formation are named Kos Plateau Tuff by Allen and Cas[58], and their source is claimed to be Kos and Nysiros Islands[59,60]. According to the results of single-crystal Ar–Ar age dating of sanidine crystals, the ages of Yazıköy pyroclastics were found to be 161 ka[61].

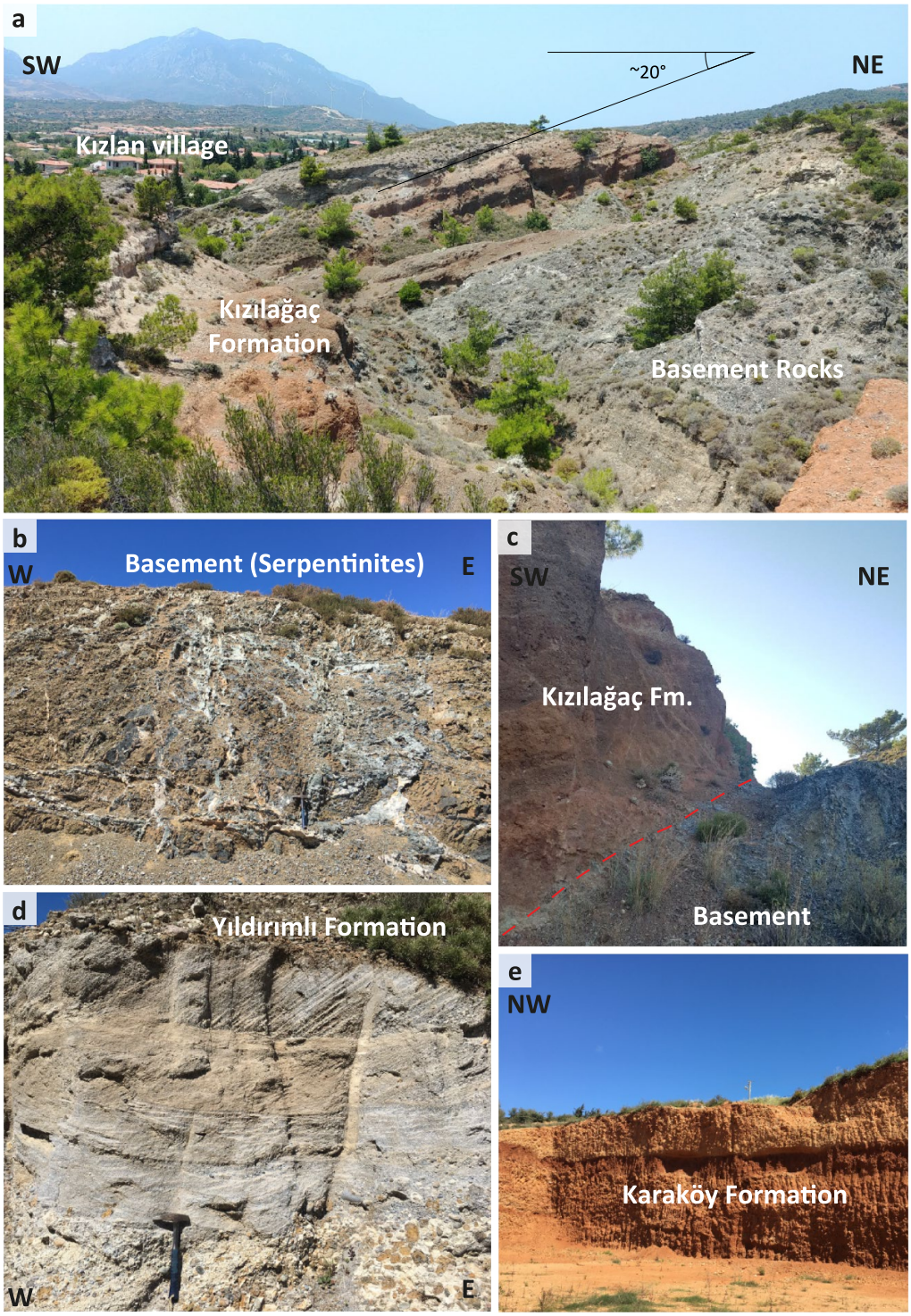


Fig. 3. Field pictures of various units in the study area. (**a**) Unconformity plane between the basement rocks and Kızılağaç Formation (NE of the Kızlan Village), note 20° south dip of the unit. (**b**) A general view of the Ophiolitic Basement rocks, (**c**) A Close-up view of the unconformity between the Ophiolitic basement and Kızılağaç Formation. (**d**) Cross-beds in the Yıldırımlı Formation, (**e**) Field view of the Karaköy Formation.

Karaköy formation At the northwest of Karaköy (Fig. 2), the Karaköy Formation is well exposed along the southern margin of Datça Graben. The formation was first named by Dirik[57] as Karaköy Formation and distinguished from other Quaternary deposits.

Karaköy Formation is recognized by its characteristic red colour, and it is nearly horizontal (Fig. 3e). Karaköy Formation, which unconformably overlies the Yıldırımlı Formation and consists of breccias with polygenetic pebbles settled in a bricky-red sandy and clayey matrix. It is deposited as marginal facies of Datça Graben since

rapid uplift and erosion took place at the western part of Reşadiye horst. Away from the southern margin, the grain size decreases, and the lithology passes into red sandstone, greenish-yellow claystone-mudstone alternation.

The early Quaternary age is assigned for the age of the Karaköy Formation since it unconformably overlies the late Piacenzian Yıldırımlı Formation[57]. However, it unconformably overlies the Yazıköy Formation, the age of the Karaköy Formation must be younger than 161 Ka.

Methods and techniques

This study integrates magnetostratigraphy, (U-Th)/He zircon geochronology, sedimentological analysis, and fault kinematic studies to constrain the stratigraphy, age, and tectonic evolution of the Datça Graben. Paleomagnetic sampling was conducted across three stratigraphic sections, with rock magnetic properties analysed to identify dominant magnetic carriers. Fault slip data were collected to reconstruct paleostress configurations, while zircon (U-Th)/He dating provided precise depositional ages for interbedded tuff layers. These multidisciplinary approaches collectively refine the chronology of the basin infill and its structural development, offering insights into regional extensional dynamics.

Structures

Datça Graben is a WNW-trending depression bounded by two normal faults in the north and the south (Fig. 2). The structures related to the evolution of the basin include the basin bounding normal faults that provided accommodation space and controlled the deposition of the basin infill, and mesoscopic faults that developed within the infill that are contemporaneous with the deposition as indicated by growth features where downthrown blocks have thicker deposits than the up thrown blocks.

The northern boundary fault is a normal fault dipping to the south and it is traceable from Kızlan to the northeast of Körmen Harbour (Fig. 2). To the east of the fault, it changes strike from E-W to NW–SE. The basement rocks and Yıldırımlı Formation juxtapose along the northeastern side of the fault. The alluvial fans and triangular facets are also observable, and they represent the recent activity of the northern boundary fault.

The southern boundary fault is composed of two segments oriented in the NW–SE direction. At Hızırşah, the eastern segment jumps to the north and continues to Datça Harbour. The total length of the fault is almost 9 km. Along the fault zone, basement rocks juxtapose with Yıldırımlı Formation and Karaköy Formation.

Paleostress analysis

To understand the kinematics of the basin controlling faults we have conducted a very extensive fault kinematic study in the region and collected 884 fault slip data.

The sampling sites were chosen structurally homogeneous and as small as possible to avoid the probable problems due to relative block and fault interactions. In general, four fault categories were determined concerning locations in the geological map and relative ages of the lithologies. These are faults located in the basement rocks, syn-sedimentary faults, and the marginal boundary faults both from the northern boundary and southern boundary of the Datça Graben. A total of 152 fault slip data were collected from the basement rocks, 416 fault slip data were collected from the basin bounding faults and the remaining 318 measurements were collected from the growth faults associated with the basin infill. The faults belonging to basement rocks are characterized mainly by compressional deformation as indicated by reverse and oblique-slip faults with reverse components. However, the basin bounding faults and other faults associated with the basin infill are dominated by normal components. These two sets are separated and analysed independently.

During sampling, for each sampling site, the attitude of the fault plane was measured together with the slickenline attitudes and the sense of motion along the fault planes (Fig. 4). The orientations of the slickenlines were measured by using the EGeo Compass Pro application developed by Marc Foi[62]. On some fault planes, reliable movement senses could not be determined. Such slip data are not included in the paleostress reconstructions.

Geochronology

During magnetostratigraphic sampling, we encountered two air-fall ash layers (tuff) within the infill of the Datça Graben. These tuff layers were carefully sampled for Zircon Helium (ZHe) dating. Specifically, we collected tuff samples from two distinct levels: one from the lower section (DLT) and another from the upper section (DUT). During the sampling process, necessary precautions are followed to ensure that the minerals are not affected by external factors such as weathering or alteration, preserving their primary properties. Additionally, the stratigraphic positions and structural context of the sampled rocks are noted.

The (U-Th)/He Zircon dating technique relies on the ratio between the half-lives of uranium and thorium isotopes and the production of alpha decay (^{4}He) over time. Notably, the ages obtained through this dating method are generally younger than the crystallization or sedimentation ages. This discrepancy arises from the time that the samples spent at temperatures higher than the closure temperature for the zircon helium system, which is approximately 180–200 °C[63].

Helium atoms become trapped within zircon crystals at temperatures below the closure temperature. Their production occurs via α-irradiation during the conversion of ^{238}U, ^{235}U, ^{232}Th, and ^{147}Sm isotopes to ^{206}Pb, ^{207}Pb, ^{208}Pb, and ^{143}Nd through radioactive decay. To calculate the ZHe age, we rely on Farley[64] and Reiners et al.[63], including the half-life constant (λ) and the amounts of ^{4}He, ^{238}U, ^{235}U, and ^{232}Th atoms preserved in the zircon crystals.

The ZHe age formula assumes the absence of primary ^{4}He in the zircon particle and is expressed as follows:

$^4\text{He} = 8^{238}\text{U}(\exp(\lambda_{238}\text{t})\text{-}1) + 7^{235}\text{U}(\exp(\lambda_{235}\text{t})\text{-}1) + 6^{232}\text{Th}(\exp(\lambda_{232}\text{t})\text{-}1)$, t = αHe age

For ZHe age calculations, the amount of ^{4}He stored in optically clean zircon crystals (free from extra mineral or fluid inclusions) is determined using a quadrupole mass spectrometer connected to a laser beam heated

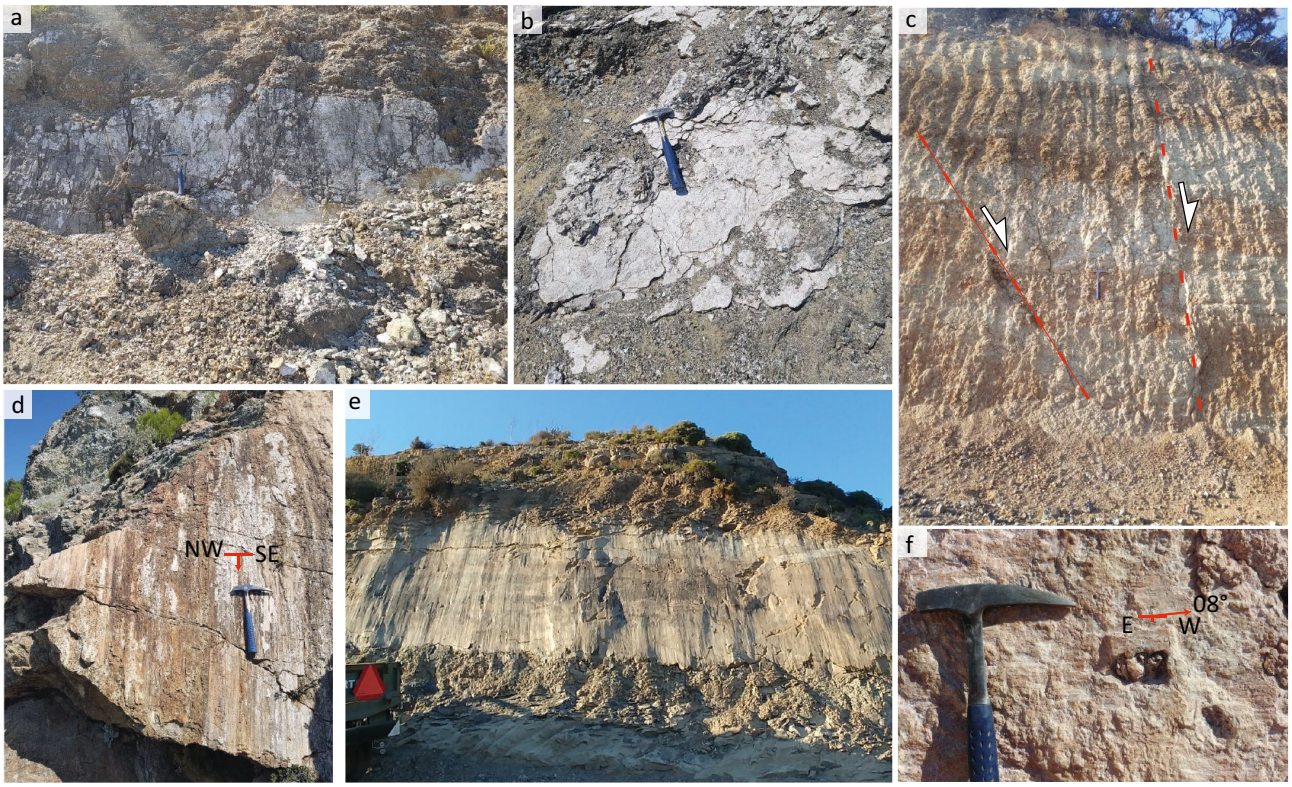


Fig. 4. Field pictures of structures encountered during field studies. (**a**) Fault plane within the basement rocks. (**b**) Close-up view of a reverse fault plane. (**c**) Syn-sedimentary growth faults developed in the Yıldırımlı Formation (**d**) Slickensides on the northern boundary fault. (**e**) Normal fault plane in the Yıldırımlı Formation. (**f**) E-W-oriented sinistral strike-slip fault plane. Arrows indicate the sense of the fault slip.

system (ALPHACHRON device at the Department of Neotectonics and Thermochronology, Institute of Rock Structure and Mechanics of the CAS). Additionally, we measured the amounts of 238U, 235U, 232Th, and 147Sm using an HS-ICP-MS (High-Resolution Inductively Coupled Plasma—Mass Spectrometer) at the Geological Institute of the Czech Academy of Sciences. Each sample was analysed from at least three zircon crystals, and the average age of these grains was assigned as the ZHe age for the corresponding sample (Table 2). The age error corresponds to the standard deviation of the three individual ages. We refer to Gülyüz et al.[25] for the full account of the methodology.

While this method provides insights into the cooling history of the samples from temperatures around 180–200 °C to surface conditions, it's essential to note that our study samples originate from tuff layers. Consequently, the obtained ages should correspond to the deposition ages of these samples.

Magnetostratigraphic sampling and analysis

Samples were collected from the infill sediments of Datça Graben from predetermined three sections named Datça Lower (DL), Datça Middle (DM), and Datça Upper (DU) (Fig. 2). A gasoline-powered drilling machine was used to obtain a standard-sized oriented paleomagnetic core sample at approximately 1 m intervals, mainly from marl and mudstone levels, occasionally from limestone and fine sandstone levels. The clay content is very high for almost all levels, a cordless compressor for air drilling was preferred instead of water flushing. All the core samples were oriented by using a magnetic compass and an inclinometer. After removing the weathered surface layer, a total of 344 cores were collected from 102 stratigraphic levels. Of these, 164 samples belong to DL (150 m.), 17 samples belong to DM (25 m.), and 163 samples belong to DU (150 m.) (Fig. 5). The total thickness of the Datça composite section is nearly 325 m. In the upper parts of the Datça Upper (DU) section, the lithology changed into unconsolidated Quaternary alluvium, from which sampling was not performed. From each level, at least three samples were collected. Bedding and sample results are corrected for present-day declination values which is about 5° according to the National Oceanic and Atmospheric Administration (NOAA) website, accessed in 2018 https://www.ngdc.noaa.gov/geomag/calculators/magcalc.shtml).

All paleomagnetic measurement procedures were carried out in Fort Hoofddijk Paleomagnetic Laboratory at Utrecht University (the Netherlands). Before measurements, drilled cylindrical samples with a diameter of 25 mm were cut into standard-sized specimens of 22 mm, nearly 10.5 mm3 volume per specimen. Twin specimens were prepared for testing at all levels by using different demagnetization procedures. The remaining parts of the core samples were crushed into powder to be used for thermomagnetic runs by using a horizontal translation-type Curie balance with a noise level of 5×10^{-9} Am2[65].

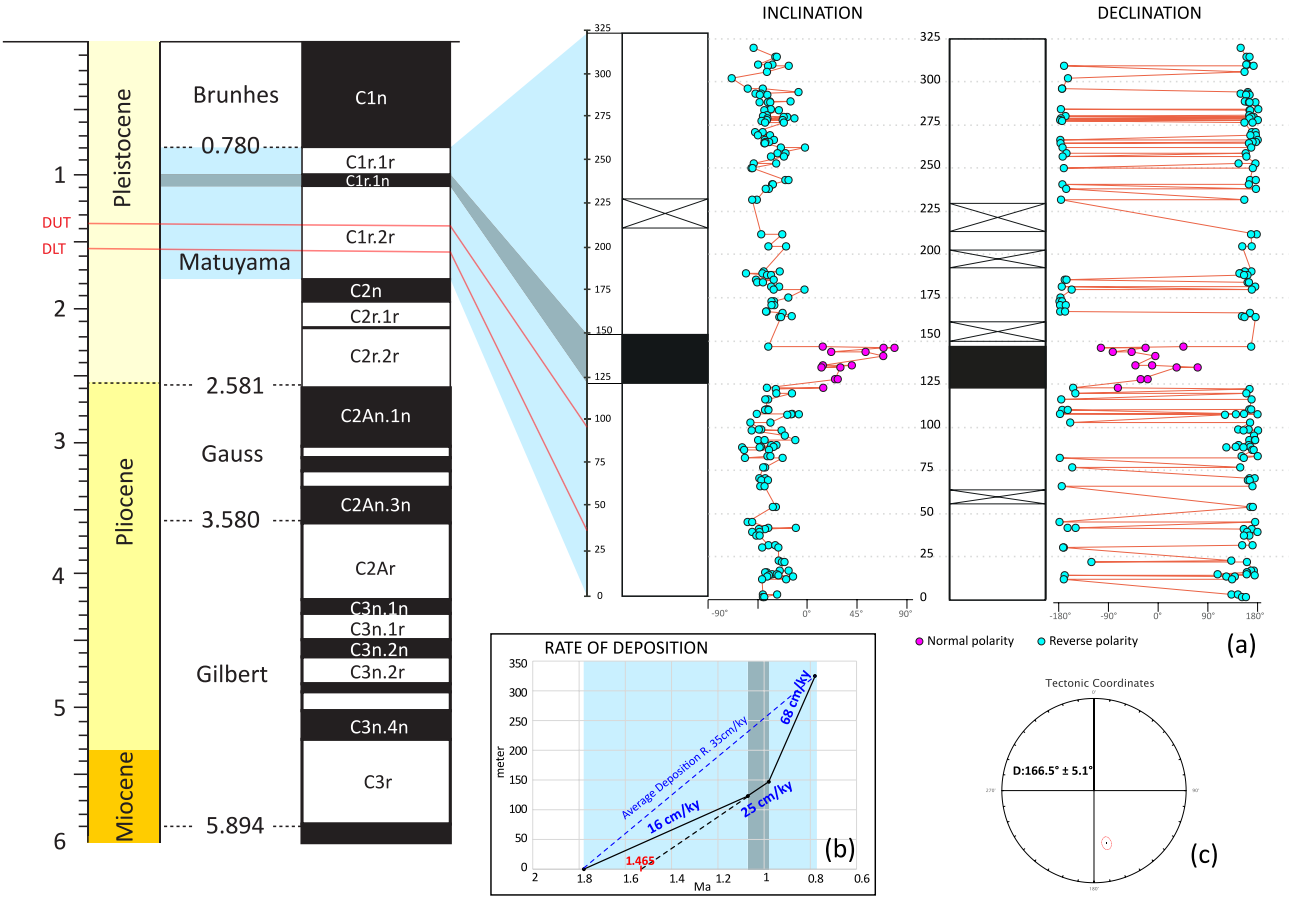


Fig. 5. (**a**) Results of paleomagnetic directions of composite Datça section and their correlation with the Geomagnetic Polarity Time Scale (GPTS)[73]. The crossed boxes are unsampled paleomagnetically unfavourable lithologic levels such as conglomerate and coarse-grained sandstone. (**c**) Result of Mean Declination and Inclination values.

For Curie balance measurements, 11 samples were chosen from all levels regarding the lithology changes. Six samples from the Datça Lower (DL) section, one sample from the Datça Middle (DM) section, and four samples from the Datça Upper (DU) section were chosen for thermomagnetic runs, and they were powdered. Almost 40 mg of powdered samples were put into a quartz glass sample holder, held between quartz wools. After that, all the samples were separately placed into a horizontal-type Curie balance measurement device. These samples were subjected to multiple heating and cooling cycles starting from the room temperature up to a maximum of 700 °C with a heating rate of approximately 6–8 °C/min and a cooling rate of 10 °C/min under the effect of 100–300 mT applied field.

Full vector magnetization measurements of stepwise demagnetization of natural remanent magnetization (NRM) for each sample were performed on a 2G Enterprises horizontal DC-Squid magnetometer with a noise level of 3×10^{-12} Am2[66]. NRM demagnetization procedure was accomplished by applying both thermal (TH) and alternating field (AF) demagnetization methods. For thermal demagnetization, 102 samples representing the whole section were thermally demagnetized in a magnetically shielded oven ($<2\times10^{-8}$T) in a stepwise increasing temperature fashion with 20–50 °C increments starting from the room temperature (20 °C) up to a maximum 580 °C depending on the maximum demagnetization temperature. Further demagnetization by heating was prohibited to avoid a new magnetic mineral formation due to thermal alteration, and for some samples, since clear intensity increase with random magnetization directions was observed before the heating step reached 580 °C, the demagnetization procedure was finished earlier. After each temperature step, the natural remanent magnetization values, both declination and inclination values for each step were measured in three components, and the measurement procedure was finished when the intensity of NRM values reached < 10% of its initial values.

Alternating field (AF) demagnetization was performed on batches consisting of 102 samples. It was achieved on a 2G Enterprises DC-Squid magnetometer with a noise level of 3×10^{-12} Am2 with attached AF demagnetization coils and an in-house built automated sample handler[66]. To perform such robotized demagnetization, all the samples should manually be placed in a Helmholtz coil to provide a non-magnetic environment for each sample, and then they put into a magnetometer for further demagnetization measurements. Before the demagnetization procedure was performed on all the samples, 16 trial samples were chosen to check whether heating of the samples

up to 150 °C would clean the magnetization gained by surface oxidation of magnetite at low temperatures, and they were demagnetized using the same magnetometer with increasing applied alternating field increments of 4–10 mT up to 100 mT. After measuring the NRM values from non-heated and heated samples, it was obtained that there was no significant change caused by the surface oxidation of magnetite to induce the magnetizations. So, all the samples were treated with AF demagnetization without heating. Selected samples representing the whole section were subjected to a stepwise increasing alternating field up to a maximum of 100 mT, and the NRM values were measured as in the case of thermal demagnetization.

Results

Results of paleostress analysis

Analysis of fault slip data was performed by using Win-Tensor (version 5.6.6) software developed by Delvaux and Sperner[67]. For the paleostress reconstructions, the R-Optimization method is applied. The obtained results include the orientation of three principal stress axes (σ1, σ2, σ3), the relative magnitudes of each principal stress, the R ratio, and the maximum angular deviation for each sampling site. Each data set is optimized at maximum using the software to a level until when no further optimization is possible[67]. The acceptable maximum angular deviation limit was kept at 30° for the computation; however, some fault planes exceeded that limit, and it became impossible to obtain reasonable results for a given fault plane. Those fault data are considered spurious and separated from the main data set. Since they may represent multiple phases of deformation or stress permutations[68,69] or they were erroneous measurements, they are discarded. The total amount of spurious data corresponds to ~ 3% of the total data. The remaining 97% of the data produced meaningful results. In total, out of 884 data from the basin bounding and growth faults, 857 fault slip data were used to construct paleostress configurations. For the results of each site see Table 1 (Supplement B).

Geochronology result

For the Datça Lower Tuff (DLT) sample, zircon grains DLT-87-2, DLT-87-3, and DLT-87-5 yielded ages of 1.45, 1.63, and 1.60 Ma, respectively. The mean of these ages is 1.56 ± 0.10 Ma, where the uncertainty represents the standard deviation of the three measurements. The same procedure was applied to the Datça Upper Tuff (DUT) sample. Zircon grains DUT-1, DUT-3, and DUT-4 yielded ages of 1.41, 1.56, and 1.37 Ma, respectively, giving a mean age of 1.44 ± 0.10 Ma (Table 2).

Paleomagnetic results

Rock magnetic properties

To better understand the dominant magnetic carriers in our samples rock magnetic studies are carried out. The Curie balance test was performed at 11 different levels, and thermomagnetic curves were obtained for each sample. Nearly all the thermomagnetic curves exhibit a gradual decrease in intensity up to approximately 645 °C, they show irreversible magnetization between 300 and 645 °C. These magnetic behaviours strongly suggest the presence of titanomagnetite, which is likely to be maghemite (γFe_2O_3). The occurrence of maghemite could also indicate a high degree of weathering associated with low-temperature oxidation[70].

The thermomagnetic curve belonging to the fine-grained mudstone sample, DL 12, shows a gradual decrease in magnetization intensity as heating proceeds up to 250 °C, and irreversible curves start to develop after ~ 350 °C. Also, a large magnetization drop occurs at that temperature and the critical Curie temperature at which the magnetic minerals lose their magnetic properties is ~ 625 °C. All these behaviours indicate the inversion of maghemite (γFe2O3) to hematite (αFe2O3).

Similarly, a thermomagnetic curve from a caliche sample (DM04) also features the same dominant magnetic carrier. However, the inflexion point is less pronounced compared to DL12, suggesting a lesser amount of maghemite-to-hematite inversion. Likewise, DL04, a siltstone sample, exhibits magnetic behaviours consistent with hematite formed from maghemite. Lastly, a thermomagnetic curve from a light-coloured fossiliferous limestone level (DU49) shares similar magnetic rock properties but with lower magnetic intensity compared to the other samples (Supplement C).

Demagnetization results

Demagnetization diagrams in the form of orthogonal vector diagrams, specifically Zijderveld diagrams are used to display the behaviours of each analysed sample. Interpretations of these diagrams were computed using the 'paleomagnetism.org' version 1.0 web page developed by Koymans et al.[71]. From the Zijderveld and equal angle stereographic (Wulff) diagrams, we extracted characteristic remanent magnetization directions for each level.

To determine magnetization directions, we employed the Principal Component Analysis (PCA) method, utilizing six to eight successive temperature or alternative field steps for thermal or alternating field demagnetization results, respectively. However, in cases where partial magnetic overprint was observed in some samples, we preferred the Great Circle (GC) method, as the PCA method did not yield reliable directions[72].

Demagnetization diagrams are categorized into three groups based on typical NRM behaviours: low-quality, medium-quality, and high-quality. In the low-quality group, very weak samples exhibited clustering Zijderveld diagrams (often referred to as 'spaghetti plots'), rendering the paleomagnetic directions unusable due to non-observable decay toward the origin. Consequently, we discarded data from these noisy samples, which constituted only ~ 2% of the total samples.

The other NRM behaviour groups yielded better results. The high-quality group displayed predominantly linear decay toward the origin, with maximum angular deviation (MAD) values less than 8°. Characteristic remanent magnetizations (ChRMs) could be plotted between temperatures of 300 and 540 °C. Given the superior stability of thermal demagnetization results compared to alternating field (AF) demagnetization, we exclusively used thermal (TH) diagrams for the high-quality group in constructing polarity patterns. The medium-quality

Site ID	Longitude	Latitude	n/nt	σ1 plunge/ trend		σ2 plunge/ trend		σ3 plunge/ trend		R
DN1	27.68923	36.77798	52/54	84	63	6	227	2	318	0.1
DN1L	27.68915	36.77797	22/23	13	200	52	93	35	299	0.43
DN2	27.68763	36.77874	18/18	69	80	19	286	9	193	0.23
DN3	27.68738	36.77824	18/19	71	340	17	132	8	225	0.17
DN3L	27.68743	36.77826	14/14	4	68	62	166	28	336	0.49
DN5	27.77861	36.78202	14/14	20	260	30	3	52	142	0.06
DN6	27.68294	36.77812	54/54	89	32	0	286	1	196	0.25
DN7	27.77714	36.78153	13/13	15	249	26	151	59	6	0.22
DN7N	27.77857	36.78191	27/27	88	297	1	63	2	153	0.4
DN7S	27.77853	36.78194	24/25	13	199	46	303	41	97	0.05
DN72	27.77694	36.78144	24/24	1	315	9	225	81	49	0.29
DN73	27.77694	36.78144	11/11	12	69	31	332	56	178	0.11
DN74	27.77694	36.78145	17/18	8	155	6	65	80	295	0.27
DN75	27.77683	36.78141	14/14	3	15	6	285	83	133	0.32
DN76	27.77791	36.78176	23/23	2	86	22	355	68	181	0.19
DN8	27.77861	36.78202	12/14	6	329	46	233	44	65	0.74
DN9	27.77875	36.78216	29/31	3	243	22	334	68	146	0.92
DN10	27.77222	36.76994	28/30	9	98	1	188	81	285	0.18
DN14	27.72613	36.77899	23/23	74	145	6	33	14	301	0.24
DN16	27.71789	36.78385	15/24	64	181	25	16	6	283	0.28
DN17	27.71791	36.78212	10/10	75	81	3	340	14	250	0.29
DN18	27.70132	36.77242	119/130	79	257	8	121	7	30	0.4
DN19	27.70540	36.77050	23/23	88	156	2	294	1	24	0.29
DN20	27.69802	36.77350	25/25	87	248	2	104	2	14	0.51
DN21	27.69693	36.77251	17/17	74	258	15	99	6	8	0.41
DN22	27.69470	36.77524	46/50	79	67	7	296	8	205	0.22
DN23	27.72611	36.77894	12/12	71	47	6	157	18	249	0.2
DN24	27.72617	36.77892	9/9	51	97	38	285	4	192	0.25
DaN1	27.71132	36.77264	19/19	81	18	6	244	6	153	0.42
DaN2	27.6784229	36.77808	9/9	57	83	10	189	31	285	0.34
DaN3	27.67846	36.77813	13/13	87	14	0	281	3	190	0.2
DaN4	27.67775	36.77939	14/14	81	111	8	260	5	350	0.28
DaN5	27.64999	36.78311	12/12	58	44	19	281	25	182	0.42
DS1	27.63298	36.74989	8/9	5	173	33	267	56	75	0.84
DS2	27.63204	36.75002	17/17	50	95	37	301	13	201	0.27
DS3	27.63611	36.74728	9/10	17	255	69	38	12	161	0.11
DS4	27.66302	36.72031	14/14	19	221	52	337	31	119	0.35
DS5	27.68348	36.72166	9/9	64	274	17	145	19	49	0.16
DS6	27.68509	36.71833	33/33	81	173	2	277	8	8	0.27
DS7	27.68554	36.71815	20/20	86	163	3	292	3	22	0.19
DS8	27.68525	36.72058	12/12	87	206	2	4	1	94	0.28
DS8S	27.68524	36.72058	20/23	15	183	47	76	39	286	0.25
DS9	27.63334	36.76889	18/18	54	59	22	296	28	194	0.49

Table 1. Locations of paleostress sites and results of each sampling site. n/nt: total sample number/used sample number, R: shape factor of stress ellipsoid $R = (\sigma_2 - \sigma_3)/(\sigma_1 - \sigma_3)$ (stress ratio).

group consisted of samples showing more scattered decay behaviour than the high-quality group. Although most samples did not fully decay toward the origin, the results remained interpretable. MAD values generally stayed below 20°, but for many TH samples, this value dipped as low as 10°.

For polarities, we relied on diagrams from both the high-quality and medium-quality groups (see Supplement C). In cases where neither TH nor AF samples exhibited high or medium-quality behaviour, we used low-quality samples to predict the general polarity pattern for those levels.

Analysing the demagnetization results from samples with mean magnetic intensity values ranging from 9.4×10^{-9} to 552.2×10^{-9} A/m, we observed that declination directions showed a random distribution for

Sample	Th/U	Moles 4 He	Moles 238 U	Moles 235 U	Moles 232 Th	Moles 147 Sm	ppm U 238	ppm U 235	ppm Th 235	ppm Sm 147	Age (Ma) (uncorrected)	Error	FT	Age (Ma) (corrected)	Average age ± st.dev
DUT-1	0.78	8E-14	5E-12	4E-14	4E-12	3E-15	499.48	3.6761	390	1.15	1.01	0.01	0.72	1.41	1.44 ± 0.1
DUT-3	0.67	2E-13	8E-12	6E-14	6E-12	3E-15	352.79	2.5945	236	0.46	1.22	0.01	0.79	1.56	
DUT-4	0.69	6E-14	4E-12	3E-14	3E-12	3E-15	630.12	4.64	433	1.80	1.01	0.01	0.74	1.37	
DLT-87-2	0.71	6E-14	4E-12	3E-14	3E-12	3E-15	227.64	1.6767	161	0.72	1.09	0.01	0.76	1.45	1.56 ± 0.1
DLT-87-3	0.56	1E-13	6E-12	4E-14	3E-12	3E-15	498.55	3.6686	279	1.13	1.26	0.01	0.77	1.63	
DLT-87-5	0.61	4E-13	2E-11	1E-13	1E-11	9E-15	357.47	2.6271	217	0.66	1.20	0.01	0.75	1.60	

Table 2. Results of (U-Th)/He Zircon dating technique.

each sample. Inclination directions mostly remained below 60°. Consequently, we conclude that the magnetic directions were not aligned parallel to the axis of the drill core during mechanical drilling.

The resulting polarity pattern was derived from the obtained demagnetization inclinations. We identified individual polarity zones, each comprising at least three successive levels with similar polarity. The levels which cannot be sampled due to high conglomerate and coarse sand-sized sediment content were represented as crossed boxes in the section. Overall, the Datça composite section revealed three recognized magneto zones. It commences with a long reverse polarity pattern, followed by a brief normal polarity interval, and concludes with a second relatively longer reverse polarity pattern (Fig. 5). Notably, the prominent polarity is reversed, particularly in the Datça Lower and Datça Upper sections.

Overall, evaluation of all of the samples from the Yıldırımlı Formation indicate that the mean declination is D: 166.5° ± 5.1° and mean Inclination is I: 41.2 ± 6.2indicating approximately 13° ± 5° counter-clockwise rotation.

Discussion

The integration of magnetostratigraphic, geochronological, and structural data from the Datça Graben reveals three key aspects of its Pleistocene evolution. These include an asymmetric half-graben development dominated by southern boundary fault activity, ~ 13° ± 5° counterclockwise rotation since the Calabrian, post-0.78 Ma uplift of the basin more than 100 m, and constraints on the opening age of the Gökova graben and inundation of the Aegean sea basin. These findings bear significant implications for understanding the interplay between regional extension, block rotation, and continental-marine transitions in the SE Aegean region. Below, we examine these results in the context of the opening of the Gökova Basin and broader Aegean tectonics.

Interpretation of the paleostress results

The paleostress configurations of the faults within the basement rocks exhibit distinct characteristics. Specifically, the maximum principal stress (σ_1) and intermediate principal stress (σ_2) are oriented horizontally, while the minimum principal stress (σ_3) is vertical. This stress configuration suggests contractional tectonics, likely associated with reverse faults that are abundant within the footwall block of the northern boundary fault in the northern margin of the Datça Graben. These faults predate the development of the Datça Graben, as they are confined exclusively to the basement rocks.

In contrast, the site associated with the infill units shows a different paleostress configuration. Here, almost north–south extensional deformation is facilitated by approximately E-W striking normal faults. The fault slip data collected from the northern and southern boundary faults, as well as syn-depositional faults, are grouped into three sets for analysis. For all three sets, the maximum principal stress (s_1) remains nearly vertical, while the intermediate (s_2) and minimum (s_3) principal stresses are horizontal. The horizontal component of s_2 varies between west-southwest (WSW) and west-northwest (WNW), while s_3 changes between north-northwest (NNW) and south-southeast (SSE). These stress orientations collectively indicate an almost north–south extensional regime in the region. Although very subtle, in the northern part of the graben, the extension direction is NNW-SSE, while it is NE-SW in the southern part, manifested by NW–SE-striking normal faults (Fig. 2). The paleostress configuration of syn-depositional faults is almost identical to the northern boundary faults with less than 10° of variation (Supplement B).

Correlation to geomagnetic polarity time scale (GPTS)

The polarity pattern obtained from the demagnetization procedure is compared with the Geomagnetic Polarity Time Scale (GPTS). For the Pleistocene polarity patterns, correlation can be made with both the C2r and C1r chrons[73], leading to an interpretive ambiguity. Since both intervals display similar reversed–normal–reversed polarity successions, making it difficult to assign the observed sequence to a unique chron. In order to overcome this discrepancy, radiometric dating results are used as reference points, correlating to 1.56 and 1.37 Ma for DLT and DUT samples, respectively. Both ages fall within the C1r.2r reversed chron within the Matuyama chron. In addition, the top and base of the analysed sections end within the reversed chrons both at the base and the top, it is not possible to date exact timing of beginning of deposition of Yıldırımlı Formation. However, it must be younger than 1.8 Ma, since it is the base C1r.2r reversed polarity. Similarly, the upper boundary of the Yıldırımlı Formation must be younger than 0.78 Ma since it is the top of the C12.1r polarity.

One viable way to determine the age of the top and bottom of the section could be using a constant deposition rate for the total duration of the normal polarity, C12.1n, since it is covered entirely by the Yıldırımlı Formation sequence (Fig. 5). In this case, the oldest part of the section would be 1.465 Ma based on 25 cm/Ky deposition rate (Fig. 5b). However, 1.465 Ma age is younger than the radiometrically dated tuff horizons, indicating that the deposition rate was variable. Since, no reliable way of determining the exact age of the base of the Yıldırımlı Formation was possible, we preferred to take the base of the C1r.2r reverse subchron as the lower limit of the age of the unit. This age implies that the sedimentation rate of the lower reversed polarity interval is about 16 cm/Kyr much lower than upper sections. Given that this section comprises dominantly lacustrine fine clastics, it is reasonable to assume that sedimentation was slower during this period.

Similarly, there is no reliable way of determining the exact age of the top of the section, we preferred to take the top of the reversed subchron, c1r.1.r, as the top of the section. During this time interval, the sedimentation rate reaches 68 cm/Kyr, likely due to the presence of thick conglomerate layers, indicating a higher sedimentation rate compared to other polarity levels. Overall, the geomagnetic polarity pattern of the Datça composite section is correlated with the C1r chron, encompassing the C1r.2r, C1r.1n, and C1r.1r subchrons, which correspond to the time interval of ~ 1.78 to ~ 0.78 Ma (Fig. 5).

Development of Datça Graben

The continental Kızılağaç Formation is exposed only in the northern part of the Datça Graben, resting unconformably on the basement rocks of the northern hanging-wall block. In contrast, at the southern margin of the graben, the basement rocks are juxtaposed with the Yıldırımlı and Karaköy formations along a buttress unconformity, indicative of fault-controlled deposition. The presence of widespread growth faults within these units further supports the occurrence of syn-depositional faulting. The faults associated with these units predominantly exhibit normal characteristics, suggesting that the accommodation space for the Yıldırımlı and Karaköy formations was facilitated by these normal faults.

The Late Pliocene Yıldırımlı and Karaköy formations dip southward as a homocline at an angle of approximately 20° (Figs. 2b, 3), indicating that the vertical displacement of the southern boundary fault is greater than that of the northern boundary fault. This asymmetry indicates the differential development of the Datça Graben during the Pleistocene (Calabrian). The absence of the Kızılağaç Formation south of the southern margin of the Datça Graben implies that its deposition was controlled by the southern basin bounding fault. Similarly, the deposition of the Yıldırımlı Formation was also controlled by the southern boundary fault before the development of the northern boundary fault, which may have been active during the deposition of the Yıldırımlı Formation, but it was not as active as the southern boundary fault. This is deduced from the field observations that there are no major facies changes within the Yıldırımlı Formation on either side of the fault, although it delimits the present geometry of the basin (Fig. 6b–d). Ersoy[49,50] and later Dirik[57] suggested that the Datça Graben evolved from a half-graben, with the southern boundary fault developed first, followed by the northern boundary fault after the deposition of the Yıldırımlı and Kızılağaç formations. Our observations concur with the sequential development of these faults, however, the role of the northern boundary fault is limited to none during the deposition of the Yıldırımlı Formation. It seems its activity became significant after the deposition of the Yıldırımlı Formation and was developed as a response to southwards differential tilting and N-S extension of the Datça Graben.

The Yıldırımlı Formation is characterized by fluvio-lacustrine environments, transitioning upwards into shallow-marine fan delta deposits, indicating at least one transgressive event during the early Pleistocene. The total vertical thickness of the Datça Graben infill is approximately 350 m, with marine deposits located towards the top of the sequence. The measured marine sequence is about 50 m thick, with its uppermost part approximately 100 m above sea level. According to Dumitru et al.[74] and Bintanja et al.[75], global sea levels during the deposition of the Datça Graben infill (1.78–0.78 Ma) were consistently lower than present-day levels. This

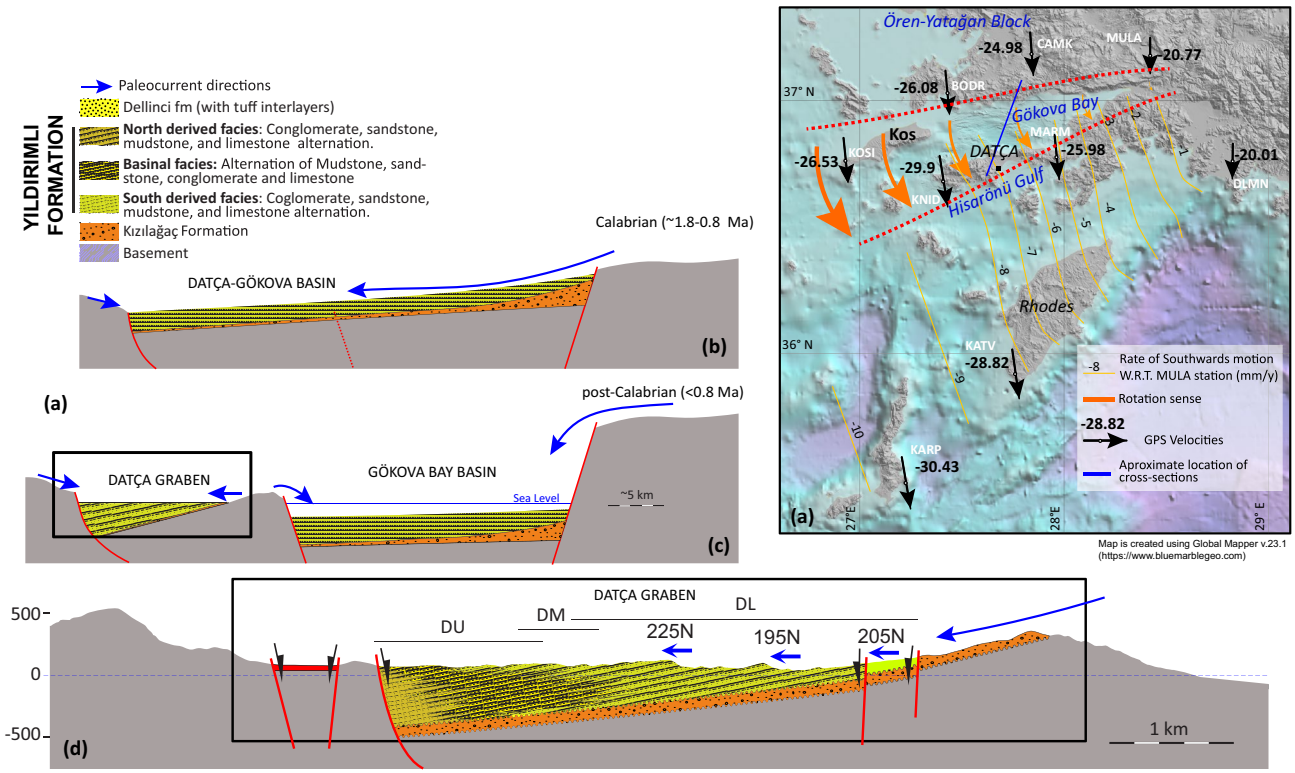


Fig. 6. (**a**) GPS velocities (Reilinger et al.[83]) showing the southwards motion of various landmasses around the study area. Red dashed lines are arbitrarily drawn to emphasize the differential motion and rotation of the blocks. Proposed evolutionary model of the Datça Graben and opening of the Gökova Bay, (**b**) during Calabrian, (**c**) post Calabrian geometry, and (**d**) close up of present geometry of Datça Graben. Bathymetric and topographic data is obtained from Gridded Bathymetric data from GEBCO-General Bathymetric Chart of the Oceans[89]. Map was created using Global Mapper v.23.1[90].

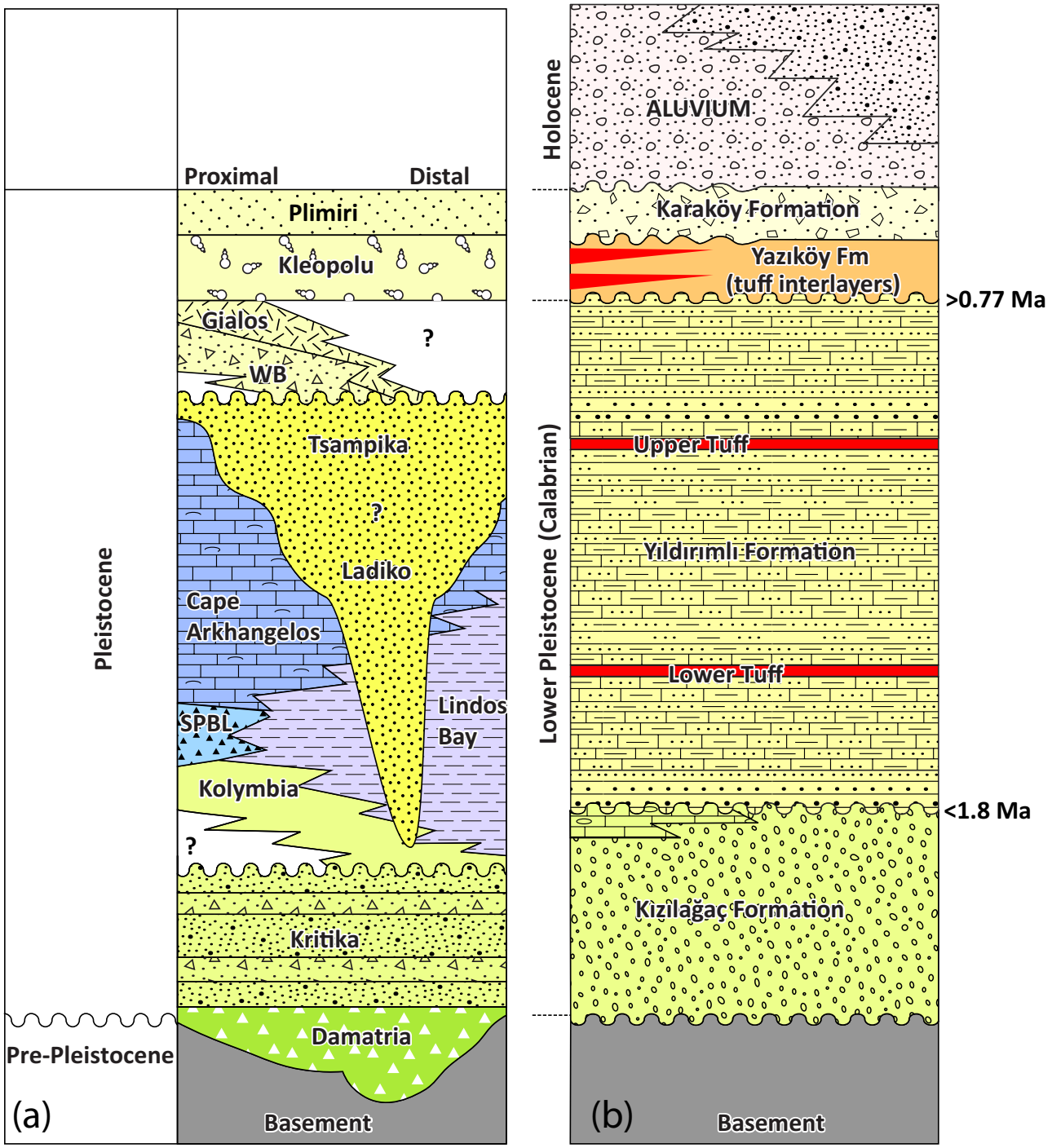


Fig. 7. Correlation of facies between (**a**) Northeast Rhodes Island[42] and (**b**) Datça Graben (this study).

implies that the Datça Peninsula must have experienced an uplift of more than 100 m after post-Calabrian Age (after ~ 0.78 Ma).

Regional implications

In this study, the mean rotation for the Datça Graben infill is estimated at ~ 13° ± 5° (D: 166.5.1° ± 5.1°, I: 41° ± 6.2°) in a counterclockwise (CCW) sense. Paleostress configurations for faults associated with the basin infill, as well as for basin-bounding faults, show a slight variation in orientation from NNW to NNE in places. Overall, these orientations indicate that the Datça Graben developed under approximately N-S extensional deformation.

Quillévéré et al.[76] reported that the Lindos Bay Formation on Rhodes Island was deposited between ~ 1.9 and 0.8 Ma, nearly the same interval as the deposition of the Yıldırımlı Formation in the Datça Graben (~ 1 Ma, Fig. 7). However, the Lindos Bay Formation was deposited mainly under marine conditions, whereas

the Yıldırımlı Formation was deposited in a fluvio-lacustrine environment with marine incursion only at its upper levels. Based on benthic foraminiferal assemblages and magnetostratigraphic dating[77], Hanken et al.[54] proposed that the Kolymbia Limestone of Rhodes Island was deposited in the early Pleistocene. Notably, initial foraminiferal occurrences there are found above the tuff layer. In the Datça Graben, foraminifera are observed only in the upper layers of the DLT and DUT tuff sequences, whereas in Rhodes they occur within marine units of the same period. This implies either higher sea levels or regional uplift affecting both locations.

According to Dumitru et al.[74] Pleistocene sea levels in the western Mediterranean and the Aegean domain[78] were almost always lower than present, a trend likely valid for the broader Mediterranean and the study area. Similarly, Van der Geer et al.[79] reported that during the late Pleistocene, several Aegean islands, including Rhodes and adjacent islands, were connected to mainland Turkey and Greece, providing land bridges for dwarf elephants. Kızıldağ et al.[80] reported that inundation of Hisarönü Gulf (Fig. 6) at the southern margin of Datça Graben and north of Rhodes Island took place during the late Pleistocene to Holocene and it is associated with tectonic movements. This suggests sea levels were already lower than today (Fig. 1). Marine deposition in the Datça Graben persisted until ~ 0.78 Ma, and these marine deposits are now uplifted to more than 100 m above present sea level. Therefore, the end of marine deposition and the uplift of the Datça Graben and its surroundings likely occurred after ~ 0.78 Ma, associated with regional tectonic uplift, possibly due to dynamic topography related to slab-edge processes along the Pliny-Strabo trenches[6,24,81].

Except for the upper ~ 100 m of marine sequences, the Datça Graben infill, over 350 m thick, was deposited in a fluvio-lacustrine environment dominated by coarse clastics and intercalated carbonates. The average deposition rate is approximately 35 cm/Ky, which is very rapid. Given the fluvio-lacustrine setting, such a high rate suggests a large catchment area and a major river system, neither of which are present in today's morphology. We therefore propose that the sediments of the basin were sourced from a highland area to the north, corresponding to the present-day location of the Gökova Graben. This implies that parts of the Gökova Bay area were above sea level during the Calabrian Age and supplied sediments to the Datça Graben. The regional topography likely sloped southward from north of Gökova Bay toward Rhodes Island[41,42].

Tur et al.[82] proposed that the Gökova Basin opened from west to east by counterclockwise rotation of the Datça Peninsula about 6°. Our paleomagnetic data show a 13° ± 5° counterclockwise rotation of the Datça Graben since Calabrian Age. Kaymakci et al.[6] reported that the Ören-Yatağan Block rotated approximately 24 ± 5° counterclockwise by the Middle Miocene. Although, it is not known how many degrees of this rotation took place since the Middle Pleistocene, however, present GPS vectors indicate an increase in the rate of the velocity field[83], from the eastern tip of the Gökova Bay westwards (Fig. 6a). Additionally, the westwards widening wedge shape of the Gökova Bay implies that there is a differential rotation between Ören-Yatağan Block and the Datça Peninsula, as suggested by Tur et al.[82]. In that case, Ören-Yatağan Block, the northern margin of Gökova Basin, must have rotated only 5° counterclockwise, while Datça Graben rotated about 13° ± 5°CCW.

Tur et al.[82] proposed that the opening age of the Gökova Basin becomes younger from west to east. According to their interpretation, the westernmost section began to open during the Pliocene and progressively become younger eastwards, with the central part opening in the Early to Middle Pleistocene. In this case, the Datça Graben must have been isolated from the Gökova Basin already during the Early Pleistocene. However, the ages proposed by Tur et al.[82] are slightly older than our results and are based on long-distance correlations and imprecise dating techniques. Although our ages do not match theirs, our data support the eastward-younging, counterclockwise rotational opening of the Gökova Bay as suggested by Tur et al.[82]. We propose that the opening of the Gökova Basin began during the Early to Middle Pleistocene, approximately ~ 2 My later than the ages proposed by Tur et al.[82].

Considering the approximately 23 km width of the Gökova Bay, along 27.75° longitude, and the duration of the opening age of the Gökova Basin which is about ~ 1 My, the N-S extension rate around Datça graben is expected to be around ~ 2.3 mm/y. Present-day GPS rates indicate a near linear increase in the N-S velocities. In the east they are generally lower, starting from 20.01 mm/y in Dalaman Station and they increase south-westwards reaching up to 32.71 mm/y west of Rhodes (Fig. 6a). Although, these rates are geologically instantaneous rates and might have been changed during the evolution of the region, however, they are important indicators of differential rotation and concur geologically and paleomagnetically[6] revealing extension rates and styles in the region.

It should be noted that there is no direct evidence, such as exposed outcrops or well data, regarding the thickness, lithology, or age of the Gökova Graben infill. All published ages[82,84,85] are based on indirect evidence. Consequently, the exact timing of the opening of the Gökova Basin remains uncertain. This study provides constraints indicating that the Gökova Basin must have begun opening after the Calabrian Age (~ 0.78 Ma).

In this context, it is also important to consider why the locus of extension shifted from the Datça Graben to the Gökova Basin. One likely explanation is the dynamic interaction between the northward-subducting African slab and the overriding southern Eurasian margin, combined with the development of the Pliny-Strabo STEP fault[6,28]. Another possible factor is regional rotation, which may have altered fault orientations, rendering previously favourable ones unfavourable. This phenomenon warrants further investigation. Finally, the sedimentation rates, proposed opening mechanism, and inferred age of the Gökova Bay suggest that marine conditions inundated parts of the Aegean Sea Basin within the last million years. The connection between the Gökova Bay and the eastern Mediterranean Sea must have occurred through the Gökova Sill (Fig. 6c). Similarly, the northern Aegean Sea Basin connected to the Mediterranean through the Lagada-Levitha and Mykonos-Ikaria sills, which lie 360–400 m below present mean sea level.

Conclusion

This study provides new and precise data for the stratigraphy and age of the infill of the Datça Graben that includes integrated analysis of magnetostratigraphy and low-temperature geochronology. It also provides

new sedimentological, structural, and kinematic information for the development of the basin that includes important insights into the regional tectonic evolution. The basin is developed under N-S-directed extensional deformation.

Magnetostratigraphic results are calibrated with radiometric ages from two tuff layers interbedded within the Yıldırımlı Formation—the main basin-fill unit—and correlated with the Geomagnetic Polarity Time Scale. The results indicate that deposition of the Yıldırımlı Formation occurred between 1.78 and 0.78 Ma. The southward-dipping, wedge-like geometry of the infill, together with the dominance of the southern boundary normal fault, indicates an asymmetric half-graben configuration. This asymmetry is reflected in thicker deposits along the southern boundary fault, with only limited input from the northern boundary fault. Regionally, comparison with contemporaneous deposits on Rhodes Island suggests that the Datça Graben represents the northernmost extent of marine inundation during the Calabrian, with increasing water depth southwards toward Rhodes. Despite their temporal overlap, the contrasting depositional environments of the Datça Graben and Rhodes Island indicate tectonic uplift and possible dynamic topography along the Pliny-Strabo trenches. Paleomagnetic evidence also supports a counterclockwise rotational opening of the Gökova Basin during Post-Calabrian Age (post ~ 0.78 Ma), highlighting differential tectonic activity across the Datça Peninsula and adjacent regions.

The observed paleostress orientations (N-S extension and rotation) align with recent GPS velocity data, highlighting a complex interplay of extensional and rotational processes. Collectively, these findings refine the tectonic history of southwestern Türkiye and contribute to broader models of Aegean extensional dynamics.

Data availability

The paleomagnetic data were processed and interpreted using the online portal https://paleomagnetism.org, where they will be accessible following publication of this manuscript.

Received: 14 May 2025; Accepted: 20 November 2025
Published online: 03 December 2025

References

1. Le Pichon, X. & Angelier, J. The Aegean sea. *Philos. Trans. R. Soc. London A* **300**, 357–372 (1981).
2. Şengör, A. M. Cross-faults and differential stretching of hanging walls in regions of low-angle normal faulting: Examples from western Turkey. *Geol. Soc. London Spec. Publ.* **28**, 575–589 (1987).
3. Taymaz, T., Jackson, J. & McKenzie, D. Active tectonics of the north and central Aegean Sea. *Geophys. J. Int.* **106**, 433–490 (1991).
4. Seyitoğlu, G. & Scott, B. Late Cenozoic crustal extension and basin formation in west Turkey. *Geol. Mag.* **128**, 155–166 (1991).
5. Bozkurt, E. Neotectonics of Turkey - a synthesis. *Geodin. Acta* **14**, 3–30 (2001).
6. Kaymakcı, N. et al. Paleomagnetic evidence for upper plate response to a STEP fault, SW Anatolia. *Earth Planet. Sci. Lett.* **498**, 101–115 (2018).
7. Özkaptan, M. et al. Deformation in SW Anatolia (Turkey) documented by anisotropy of magnetic susceptibility data. *Tectonics* **40**, e2021TC006882 (2021).
8. Dewey, J. F. & Şengör, A. M. Aegean and surrounding regions: Complex multiplate and continuum tectonics in a convergent zone. *Geol. Soc. Am. Bull.* **90**, 84–92 (1979).
9. Şengör, A. M., Görür, N. & Şaroğlu, F. Strike-slip faulting and related basin formation in zones of tectonic escape: Turkey as a case study. *Soc. Econ. Paleontol. Mineral. Spec. Publ.* **37**, 227–264 (1985).
10. Whitney, D. L. et al. Breaking plates: Creation of the East Anatolian fault, the Anatolian plate, and a tectonic escape system. *Geology* **51**, 673–677 (2023).
11. Moores, E. M., Robinson, P. T., Malpas, J. & Xenophonotos, C. Model for the origin of the Troodos massif, Cyprus, and other Mideast ophiolites. *Geology* **12**, 500–503 (1984).
12. Royden, L. H. The tectonic expression slab pull at continental convergent boundaries. *Tectonics* **12**, 303–325 (1993).
13. Govers, R. & Fichtner, A. Signature of slab fragmentation beneath Anatolia from full-waveform tomography. *Earth Planet. Sci. Lett.* **450**, 10–19 (2016).
14. Howell, A. et al. Subduction and vertical coastal motions in the eastern Mediterranean. *Geophys. J. Int.* **211**, 593–620 (2017).
15. Wortel, M. J. R. & Spakman, W. Subduction and slab detachment in the Mediterranean-Carpathian region. *Science* **290**, 1910–1917 (2000).
16. Faccenna, C. et al. Slab detachment beneath eastern Anatolia: A possible cause for the formation of the North Anatolian fault. *Earth Planet. Sci. Lett.* **242**, 85–97 (2006).
17. van Hinsbergen, D. J. J. et al. Reconciling the geological history of western Turkey with plate circuits and mantle tomography. *Earth Planet. Sci. Lett.* **297**, 674–686 (2010).
18. Biryol, C. B. et al. Segmented African lithosphere beneath the Anatolian region inferred from teleseismic P-wave tomography. *Geophys. J. Int.* **184**, 1037–1057 (2011).
19. Jolivet, L. et al. Aegean tectonics: Strain localisation, slab tearing and trench retreat. *Tectonophysics* **597**, 1–33 (2013).
20. Govers, R. & Wortel, M. J. R. Lithosphere tearing at STEP faults: Response to edges of subduction zones. *Earth Planet. Sci. Lett.* **236**, 505–523 (2005).
21. Uzel, B. et al. Paleomagnetic evidence for an inverse rotation history of Western Anatolia during the exhumation of Menderes core complex. *Earth Planet. Sci. Lett.* **414**, 108–125 (2015).
22. Uzel, B. et al. Miocene geochronology and stratigraphy of western Anatolia: Insights from new Ar/Ar dataset. *Lithos* **352–353**, 105305 (2020).
23. Özkaptan, M. et al. Age and kinematics of the Burdur Basin: Inferences for the existence of the Fethiye Burdur Fault Zone in SW Anatolia (Turkey). *Tectonophysics* **744**, 256–274 (2018).
24. Tosun, L. et al. Active tectonics and kinematics of Fethiye-Göcek Bay, SW Turkey: Insight about the eastern edge of Pliny-Strabo Trenches. *J. Struct. Geol.* **145**, 104287 (2021).
25. Gülyüz, N. et al. Low temperature thermochronology reveals tilting of crystalline bodies, Halilaga porphyry Cu-Au deposit, NW Anatolia: Implications for exploration of porphyry copper deposits and interpretation of low-temperature thermochronology data for regional tectonics. *Ore Geol. Rev.* **166**, 105958 (2024).
26. Duermeijer, C. E. et al. Post-early Messinian counterclockwise rotations on Crete: implications for Late Miocene to Recent kinematics of the southern Hellenic arc. *Tectonophysics* **298**, 177–189 (1998).
27. Duermeijer, C. E. et al. Neogene evolution of the Aegean arc: paleomagnetic and geodetic evidence for a rapid and young rotation phase. *Earth Planet. Sci. Lett.* **176**, 509–525 (2000).

28. Özbakır, A. D. et al. The Pliny-Strabo trench region: A large shear zone resulting from slab tearing. *Earth Planet. Sci. Lett.* **375**, 188–195 (2013).
29. Jolivet, L. et al. Geodynamic evolution of a wide plate boundary in the Western Mediterranean, near-field versus far-field interactions. *BSGF Earth Sci. Bull.* **192**, 48 (2021).
30. Gessner, K. et al. An active bivergent rolling-hinge detachment system: Central Menderes metamorphic core complex in western Turkey. *Geology* **29**, 611–614 (2001).
31. Thomson, S. N. & Ring, U. Thermochronologic evaluation of postcollision extension in the Anatolide orogen, western Turkey. *Tectonics* **25**, TC3005 (2006).
32. Bozkurt, E. & Park, R. G. Southern Menderes Massif: an incipient metamorphic core complex in western Anatolia, Turkey. *J. Geol. Soc. London* **151**, 213–216 (1994).
33. Bozkurt, E. Timing of extension on the Büyük Menderes Graben, western Turkey, and its tectonic implications. *Geol. Soc. London Spec. Publ.* **173**, 385–403 (2000).
34. Bozkurt, E. & Oberhänsli, R. Menderes Massif (western Turkey): structural, metamorphic and magmatic evolution-a synthesis. *Int. J. Earth Sci.* **89**, 679–708 (2001).
35. Krijgsman, W. et al. Changing seas in the late Miocene Northern Aegean: A Paratethyan approach to Mediterranean basin evolution. *Earth Sci. Rev.* **210**, 103386 (2020).
36. Palcu, D. V. et al. Late Miocene megalake regressions in Eurasia. *Sci. Rep.* **11**, 11471 (2021).
37. Grothe, A. et al. Paratethys pacing of the Messinian Salinity Crisis: Low salinity waters contributing to gypsum precipitation?. *Earth Planet. Sci. Lett.* **532**, 116029 (2020).
38. Van Baak, C. G. C. et al. Paratethys response to the Messinian salinity crisis. *Earth Sci. Rev.* **172**, 193–223 (2017).
39. Brueckner, H. Coastal changes in western Turkey; rapid delta progradation in historical times. *Bull. Inst. Océanogr. Monaco Spèc.* **17**, 63–74 (1997).
40. Müllenhoff, M. et al. The evolution of Lake Bafa (Western Turkey)-Sedimentological, microfaunal and palynological results. *Coastline Rep.* **1**, 55–66 (2004).
41. Cornée, J. J. et al. Tectonic and climatic controls on coastal sedimentation: The Late Pliocene-Middle Pleistocene of northeastern Rhodes, Greece. *Sediment. Geol.* **187**, 159–181 (2006).
42. Cornée, J. J. et al. Tectonic motion in oblique subduction forearcs: Insights from the revisited middle and upper Pleistocene deposits of Rhodes, Greece. *J. Geol. Soc. London* **176**, 78–96 (2019).
43. Titschack, J., Bromley, R. G. & Freiwald, A. Plio-Pleistocene cliff-bound, wedge- shaped, warm-temperate carbonate deposits from Rhodes (Greece): sedimentology and facies. *Sediment. Geol.* **180**, 29–56 (2005).
44. Titschack, J. et al. Sedimentary evolution of a Late Pleistocene temperate red algal reef (Coralligène) on Rhodes, Greece: Correlation with global sea-level fluctuations. *Sedimentology* **55**, 1747–1776 (2008).
45. Titschack, J. et al. Record of a tectonically-controlled regression captured by changes in carbonate skeletal associations on a structured island shelf (mid-Pleistocene, Rhodes, Greece). *Sediment. Geol.* **283**, 15–33 (2013).
46. Woodside, J. et al. The Rhodes Basin, a post-Miocene tectonic trough. *Mar. Geol.* **165**, 1–12 (2000).
47. Avrithis, A. I. & Fischer, W. The Late Pliocene/Early Pleistocene marine mollusc deposit of Selemonachi, Kos (Greece). *Nachrichtenblatt Ersten Vorarlberger Malakologischen Gesellschaft* **28**, 91–96 (2021).
48. Lykousis, V. Sea-level changes and shelf break prograding sequences during the last 400 ka in the Aegean margins: Subsidence rates and palaeogeographic implications. *Cont. Shelf Res.* **29**, 2037–2044 (2009).
49. Ersoy, Ş. Stratigraphy and tectonics of the neotectonic units in the Reşadiye (Datça) Peninsula, SW Turkey. *IESCA Proc.* **2**, 116–128 (1990).
50. Ersoy, Ş. Datça (Muğla) Yarımadasının stratigrafisi ve tektoniği. *Türkiye Jeoloji Bülteni* **34**, 1–14 (1991).
51. Rossi, L. A. *La Geologia della Peninsula di Datça (Turchia)* (Univ. Milano, 1966).
52. Mutti, E., Orombelli, G. & Pozzi, R. Geological studies on the Dodecanese islands (Aegean Sea). IX Geological map of the island of Rhodes (Greece): Explanatory notes. *Ann. Géol. Pays Hellén.* **22**, 79–226 (1970).
53. Meulenkamp, J. E. et al. On the Hellenic subduction zone and the geodynamic evolution of Crete since the late Middle Miocene. *Tectonophysics* **146**, 203–215 (1988).
54. Hanken, N., Bromley, R. G. & Miller, J. Plio-Pleistocene sedimentation in coastal grabens, north-east Rhodes, Greece. *Geol. J.* **31**, 393–418 (1996).
55. Kaaden, G. V. D. & Metz, K. Datça-Muğla-Dalaman çayı (SW Anadolu) arasındaki bölgenin jeolojisi. *Türkiye Jeoloji Kurumu Bülteni* **5**, 71–171 (1954).
56. Kapan-Yeşilyurt, S. & Taner, G. Datça yarımadasının geç Pliyosen pelecypoda ve gastropoda faunası ve stratigrafisi (Muğla-Güneybatı Anadolu). *MTA Dergisi* **125**, 89–120 (2002).
57. Dirik, K. Neotectonic characteristics and seismicity of the Reşadiye Peninsula and surrounding area, Southwest Anatolia. *Geol. Bull. Turkey* **50**, 130–149 (2007).
58. Allen, S. R. & Cas, R. A. F. Transport of pyroclastic flows across the sea during the explosive, rhyolitic eruption of the Kos Plateau Tuff, Greece. *Bull. Volcanol.* **62**, 441–456 (2001).
59. Gençalioğlu-Kuşcu, G. & Uslular, G. Geochemical characterization of mid-distal Nisyros tephra on Datça peninsula (southwestern Anatolia). *J. Volcanol. Geotherm. Res.* **354**, 13–28 (2018).
60. Gençalioğlu-Kuşcu, G. et al. U-Th disequilibrium, (U-Th)/He and 40Ar/39Ar geochronology of distal Nisyros Kyra tephra deposits on Datça peninsula (SW Anatolia). *Quat. Geochronol.* **55**, 101033 (2020).
61. Smith, P. E. et al. Single crystal Ar-Ar dating of a Late Quaternary paroxysm on Kos, Greece: Concordance of terrestrial and marine ages. *Geophys. Res. Lett.* **23**, 3047–3050 (1996).
62. Foi, M. *eGEO Compass Pro. An Android Application for Measuring Fault Slip Data* (Middle East Technical University, 2016).
63. Reiners, P. W., Farley, K. A. & Hickes, H. J. He diffusion and (U-Th)/He thermochronometry of zircon: initial results from Fish Canyon Tuff and Gold Butte. *Tectonophysics* **349**, 297–308 (2002).
64. Farley, K. A. (U-Th)/He dating: Techniques, calibrations, and applications. *Rev. Mineral. Geochem.* **47**, 819–844 (2002).
65. Mullender, T. A. T., Velzen, A. J. & Dekkers, M. J. Continuous drift correction and separate identification of ferrimagnetic and paramagnetic contributions in thermomagnetic runs. *Geophys. J. Int.* **114**, 663–672 (1993).
66. Mullender, T. A. T. et al. Automated paleomagnetic and rock magnetic data acquisition with an in-line horizontal "2G" system. *Geochem. Geophys. Geosyst.* **17**, 3546–3559 (2016).
67. Delvaux, D. & Sperner, B. New aspects of tectonic stress inversion with reference to the TENSOR program. *Geol. Soc. London Spec. Publ.* **212**, 75–100 (2003).
68. Homberg, C. et al. Structural inheritance and cenozoic stress fields in the Jura fold-and-thrust belt (France). *Tectonophysics* **357**, 137–158 (2002).
69. Hu, J. & Angelier, J. Stress permutations: Three-dimensional distinct element analysis accounts for a common phenomenon in brittle tectonics. *J. Geophys. Res. Solid Earth* **109**, B09403 (2004).
70. Dunlop, D. J. & Özdemir, Ö. Correction to "Crystallization remanent magnetization during the transformation of maghemite to hematite" by Özden Özdemir and David. *J. Dunlop. J. Geophys. Res.* **93**, 12216 (1988).
71. Koymans, M. R. et al. Paleomagnetism.org: An online multi-platform open source environment for paleomagnetic data analysis. *Comput. Geosci.* **93**, 127–137 (2016).

72. McFadden, P. L. & McElhinny, M. W. The combined analysis of remagnetization circles and direct observations in palaeomagnetism. *Earth Planet. Sci. Lett.* **87**, 161–172 (1988).
73. Hilgen, F. J., Lourens, L. J. & van Dam, J. A. The neogene period. In *The Geologic Time Scale* (eds Gradstein, F. M. et al.) 923–978 (Elsevier, 2012).
74. Dumitru, O. A. et al. Sea-level stands from the Western Mediterranean over the past 6.5 million years. *Sci. Rep.* **11**, 261 (2021).
75. Bintanja, R., Van De Wal, R. S. W. & Oerlemans, J. Modelled atmospheric temperatures and global sea levels over the past million years. *Nature* **437**, 125–128 (2005).
76. Quillévéré, F. et al. Chronostratigraphy of uplifted quaternary hemipelagic deposits from the Dodecanese island of Rhodes (Greece). *Quat. Res.* **86**, 79–94 (2016).
77. Løvlie, R., Støle, G. & Spjeldnæs, N. Magnetic polarity stratigraphy of Pliocene-Pleistocene marine sediments from Rhodos, eastern Mediterranean. *Phys. Earth Planet. Inter.* **54**, 340–352 (1989).
78. Lykousis, V., Roussakis, G. & Sakellariou, D. Slope failures and stability analysis of shallow water prodeltas in the active margins of Western Greece, northeastern Mediterranean Sea. *Int. J. Earth Sci.* **98**, 807–822 (2009).
79. Van der Geer, A. A. E. et al. A dwarf elephant and a rock mouse on Naxos (Cyclades, Greece) with a revision of the palaeozoogeography of the Cycladic Islands (Greece) during the Pleistocene. *Palaeogeogr. Palaeoclimatol. Palaeoecol.* **404**, 133–144 (2014).
80. Kızıldağ, N., Özdas, A. H. & Uluğ, A. Late Pleistocene and Holocene sea level changes in the Hisarönü Gulf, Southeast Aegean Sea. *Geoarchaeology* **27**, 220–236 (2012).
81. Bocchini, G. M. et al. Tearing, segmentation, and backstepping of subduction in the Aegean: New insights from seismicity. *Tectonophysics* **734**, 96–118 (2018).
82. Tur, H. et al. Pliocene-quaternary tectonic evolution of the Gulf of Gökova, southwest Turkey. *Tectonophysics* **638**, 158–176 (2015).
83. Reilinger, R. et al. Geodetic constraints on the tectonic evolution of the Aegean region and strain accumulation along the Hellenic subduction zone. *Tectonophysics* **488**, 22–30 (2010).
84. Görür, N. et al. Rift formation in the Gökova region, southwest Anatolia: Implications for the opening of the Aegean Sea. *Geol. Mag.* **132**, 637–650 (1995).
85. İşcan, Y., Tur, H. & Gökaşan, E. Morphologic and seismic features of the Gulf of Gökova, SW Anatolia: Evidence of strike-slip faulting with compression in the Aegean extensional regime. *Geo Mar. Lett.* **33**, 31–48 (2013).
86. Leite, O. & Mascle, J. Geological structures on the south Cretan continental margin and Hellenic Trench (eastern Mediterranean). *Mar. Geol.* **49**, 199–223 (1982).
87. Ten Veen, J. H. & Kleinspehn, K. L. Incipient continental collision and plate-boundary curvature: Late Pliocene-Holocene transtensional Hellenic forearc, Crete, Greece. *J. Geol. Soc. London* **160**, 161–181 (2003).
88. Ganas, A., Oikonomou, I. A. & Tsimi, C. NOA faults: A digital database for active faults in Greece. *Bull. Geol. Soc. Greece* **47**, 518–530 (2013).
89. GEBCO Bathymetric Compilation Group. The GEBCO_2025 Grid - a continuous terrain model of the global oceans and land. https://www.gebco.net. (2025).
90. Blue Marble Geographics, Global Mapper 23.1 https://www.bluemarblegeo.com/global-mapper/.

Acknowledgements

We would like to thank Levent Tosun and Fatih Seçkin Şiş for their help during fieldwork. This study is supported by TUBITAK (Project Grant No: 117R012). Bathymetric data of Gökova Bay is provided by General Directorate of Mapping of Türkiye. None of the authors have any conflict of interest with any organisations or individuals.

Author contributions

NK, CL, BU, OS: conceived and designed the study. MDI, NK, CL, BU, EK, MS, EK: collected and processed the data. MDI, CL, EG: performed the analysis. MDI: wrote the initial manuscript draft. MDI, NK, CL: contributed to interpretation of the results. NK: revised the manuscript. All the authors approved the final version.

Declarations

Competing interests

The authors declare no competing interests.

Additional information

Supplementary Information The online version contains supplementary material available at https://doi.org/10.1038/s41598-025-30011-7.

Correspondence and requests for materials should be addressed to N.K.

Reprints and permissions information is available at www.nature.com/reprints.

Publisher's note Springer Nature remains neutral with regard to jurisdictional claims in published maps and institutional affiliations.

Open Access This article is licensed under a Creative Commons Attribution-NonCommercial-NoDerivatives 4.0 International License, which permits any non-commercial use, sharing, distribution and reproduction in any medium or format, as long as you give appropriate credit to the original author(s) and the source, provide a link to the Creative Commons licence, and indicate if you modified the licensed material. You do not have permission under this licence to share adapted material derived from this article or parts of it. The images or other third party material in this article are included in the article's Creative Commons licence, unless indicated otherwise in a credit line to the material. If material is not included in the article's Creative Commons licence and your intended use is not permitted by statutory regulation or exceeds the permitted use, you will need to obtain permission directly from the copyright holder. To view a copy of this licence, visit http://creativecommons.org/licenses/by-nc-nd/4.0/.

© The Author(s) 2025